Field monitoring and numerical simulation of the thermal actions of a supertall structure

J. Z. Su[1, 2], Y. Xia[2*], Y. Q. Ni[2], L. R. Zhou[3], and C. Su[3]

[1]*College of Civil Engineering, Fuzhou University, Fuzhou, China*

[2]*Department of Civil and Environmental Engineering, The Hong Kong Polytechnic University, Hung Hom, Kowloon, Hong Kong*

[3]*School of Civil and Transportation Engineering, South China University of Technology, Guangzhou, China*

[*]Corresponding author: ceyxia@polyu.edu.hk

SUMMARY

Structural temperature is an important loading that must be considered during the design, construction, and safety assessment. The thermal action of supertall structures has rarely been investigated because of insufficient real measurement data, as compared with that on bridges. In this study, the thermal action of the 600 m-tall Canton Tower is investigated on the basis of the comprehensive long-term structural health monitoring system installed on the structure and the numerical simulation. First, the temperature model of the entire structure is derived by using the field monitoring and numerical heat transfer analysis data. In particular, (1) the temperature difference between different facades of the inner tube, (2) the temperature difference profile of the outer tube, and (3) the distribution of the temperature difference between the inner and outer tubes along the structural height are presented in detail. Results show that the nonuniform distribution of the temperature field between the different components of the structure is significant and should be carefully considered in the analysis of such a complex supertall structure. Second, the temperature effects on structural displacement, stress, and internal forces consisting of (1) the tower top horizontal displacement during different seasons, (2) the stresses of different levels/components, and (3) the bending moments/shear forces along the structural height are investigated. The simulated results obtained by using the global finite element model of the tower are verified through a comparison with the measurements. This study provides first-hand data for the design of

supertall structures in the tropical region of China.

KEY WORDS: supertall structure, thermal action, field measurement, heat transfer analysis, condition monitoring.

1. INTRODUCTION

In recent years, numerous supertall structures over 600 m tall have been built or are being constructed for commercial and residential functions in many urbanized cities of Asia. The main components of several supertall structures are placed on or outside the curtain wall. The radiation and daily temperature fluctuations have a significant effect on the overall deflection and stresses, as well as the structural vibration characteristics, of these large-scale structures because of the indeterminacy and nonuniform distribution of temperature [1–4]. For a supertall structure, the temperature-induced daily movement may be similar to or even larger than the typhoon-induced motion [5].

The cross-sectional temperature distribution within an individual structural element consists of four essential components, namely, a uniform temperature component, linearly varying temperature difference components in two transversal directions, and a nonlinear component [6]. The uniform temperature component may cause longitudinal deformation, whereas the linear temperature difference component may cause the curvature of the member. When the deformation is partially or fully constrained, internal forces occur in the member.

In the past decades, extensive studies on the temperature effects on bridges have been conducted [7, 8]. By contrast, investigations of tall buildings are limited because of the uniqueness of the construction site and structural configuration, which causes difficulty in drawing general conclusions. Since the 1970s, temperature effects on tall steel-framed buildings have been analyzed [9–11]. Analysis methods for determining the member forces and joint displacements of steel frames due to specific temperature changes in the exterior columns have been developed. Long-term observations of the temperature-induced stress on a 198 m-high TV tower have been conducted [12]. The results revealed that the stresses resulting from temperature changes were not negligible and were nonuniform along the

circumference of the cross-section of the tower. Tamura et al. [13] employed a real-time kinematic global positioning system (GPS) to measure the temperature-induced deformation of a 108 m-high steel tower on a fine weather day. The results indicated that the top of the tower remained still before sunrise, started to move northwest by approximately 4 cm after sunrise, and returned to its original position after sunset. Seco et al. [14] continuously monitored a 30 m-tall concrete building to quantify the relationship between the environmental condition and the building movement statistically. The observed displacement was consistent with the expected displacement as a function of the movement of the sun throughout the day. Breuer and his co-investigators [15, 16] investigated the temperature distribution of the Stuttgart TV Tower (212 m high) and measured the displacements caused by the combined influence of solar radiation and daily air temperature variation during different seasons and weather conditions. The temperature distribution on the external surface of the TV shaft varied with environmental conditions. The moving path of the tower top described an ellipse related to the position of the sun during a sunny day. Azkune et al. [17] indicated that the ambient temperature variation was the determining factor in load redistribution between any two consecutive construction steps of high-rise structures. Zheng et al. [18] conducted a finite element (FE) model analysis and showed that the effect of the sunshine temperature difference on the Shanghai Tower was significant.

Although field measurement on some highrise structures has been conducted, the actual temperature distribution of and the associated temperature effects on supertall structures over 300 m have not been investigated. The shortage of field measurement data regarding the thermal action of supertall structures in China leads to only simple specifications in the Chinese national standard [19] regarding this issue. In particular, the standard only specifies the uniform temperature component but has no clauses on the temperature difference among different members. The comprehensive long-term structural health monitoring (SHM) system on the 600 m-tall Canton Tower provides a good opportunity for monitoring the temperature distribution of the structure and its thermal-induced responses during the construction and service stages. In this study, the long-term monitoring data of the Canton Tower over seven years from 2008 to 2014 will be employed to investigate the aforementioned topic. Field monitoring and numerical analysis are integrated to provide a holistic investigation of the

thermal actions of supertall structures.

2. CANTON TOWER AND THE DEPLOYMENT OF TEMPERATURE SENSORS

2.1. Canton Tower

As illustrated in Figure 1, the Canton Tower is a typical supertall tube-in-tube structure with a total height of 600 m, consisting of a reinforced concrete (RC) inner tube and a steel outer tube [20, 21]. A total of 37 functional floors and four levels of connection girders link the inner tube to the outer tube. These functional floors have various functions, including TV and radio signal transmission facilities, open-air skywalk, offices, and entertainment facilities.

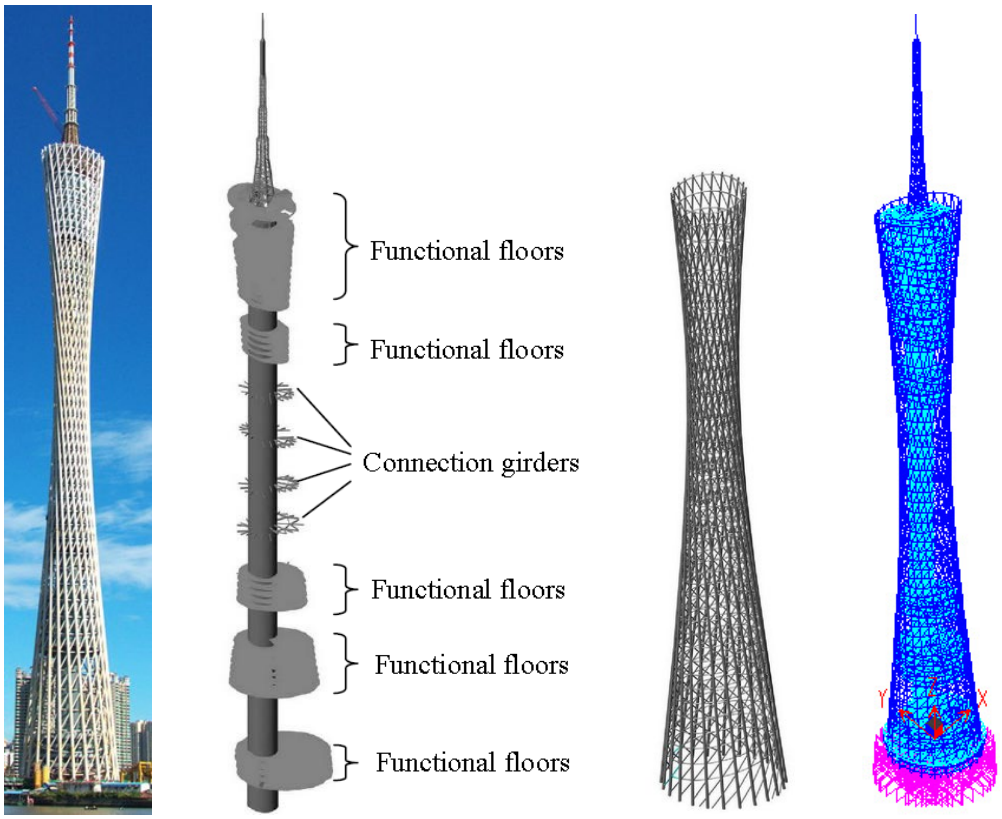

(a) (b) (c) (d)

Figure 1. Canton Tower: (a) bird's-eye view, (b) inner tube, (c) outer tube, and (d) FE model

In the structure, the segments with functional floors are enclosed by a curtain wall, such that solar radiation does not directly reach the inner tube of those parts. By contrast, the entire

outer tube and the section of the inner tube without functional floors are exposed to ambient air and solar radiation directly. Therefore, the inner and outer tubes are subjected to different thermal loadings.

The inner tube is an RC core wall made of an elliptical cross-section with a constant planar dimension of 14 m × 17 m. The outer structure consists of 24 concrete-filled tube (CFT) columns uniformly spaced in an ellipse configuration and inclined in the vertical direction, which are transversely interconnected by steel ring beams and bracings. The steel columns, beams, and bracings are coated with several layers of paint approximately 1 mm thick in total. The white paint has a low absorptivity coefficient (0.2–0.3) [22] and a low thermal conductivity, providing the steel components with a good temperature isolation from the ambient temperature environment. The planar ellipse decreases from 50 m × 80 m at the ground to the minimum of 20.65 m × 27.5 m at the "waist" level (280 m high) and then increases to 41 m × 55 m at the top of the tube (454 m).

The global FE model of the Canton Tower was constructed by using the general FE software package SAP2000 version 14.0 [23]. The full FE model of the Canton Tower is shown in Figure 1(d). In this model, four-node and three-node area elements with six degrees of freedom (DOFs) at each node are employed for the shear walls of the inner tube and the floor decks. Two-node three-dimensional beam elements with six DOFs at each node are used to model the outer tube members, the connection girders between the inner and outer tubes, and the antenna mast. All of the nodes in the basement are fixed in all directions. The full model contains 43,067 elements and 28,305 nodes in total.

2.2. Temperature and strain/stress monitoring system

Figure 2 illustrates the deployment of temperature and strain sensors on the inner RC structure and the outer CFT columns of the Canton Tower. A total of 12 cross-sections at different heights have been selected for temperature monitoring. These cross-sections correspond to the concrete inner core wall at elevations of 32.8, 100.4, 121.2, 173.2, 204.4, 230.4, 272.0, 303.2, 334.4, 355.2, 386.4, and 438.4 m and the corresponding ring nos. 3, 9, 11, 17, 21, 24, 28, 32, 35, 38, 40, and 45 at the outer tubular structure. In addition to these temperature sensors on

the structure, two more temperature sensors, one above the ground (around Section 1) and the other at the top of the tower (from the weather station), are used to measure the ambient temperature. The sections also comprise other types of sensors, such as accelerometers and anemometers, which are not shown here for brevity. Ni et al. [21] provides the description of the complete SHM system. One substation is installed at each section to collect data from all sensors in or around the section. All substations are connected together to the central data warehouse.

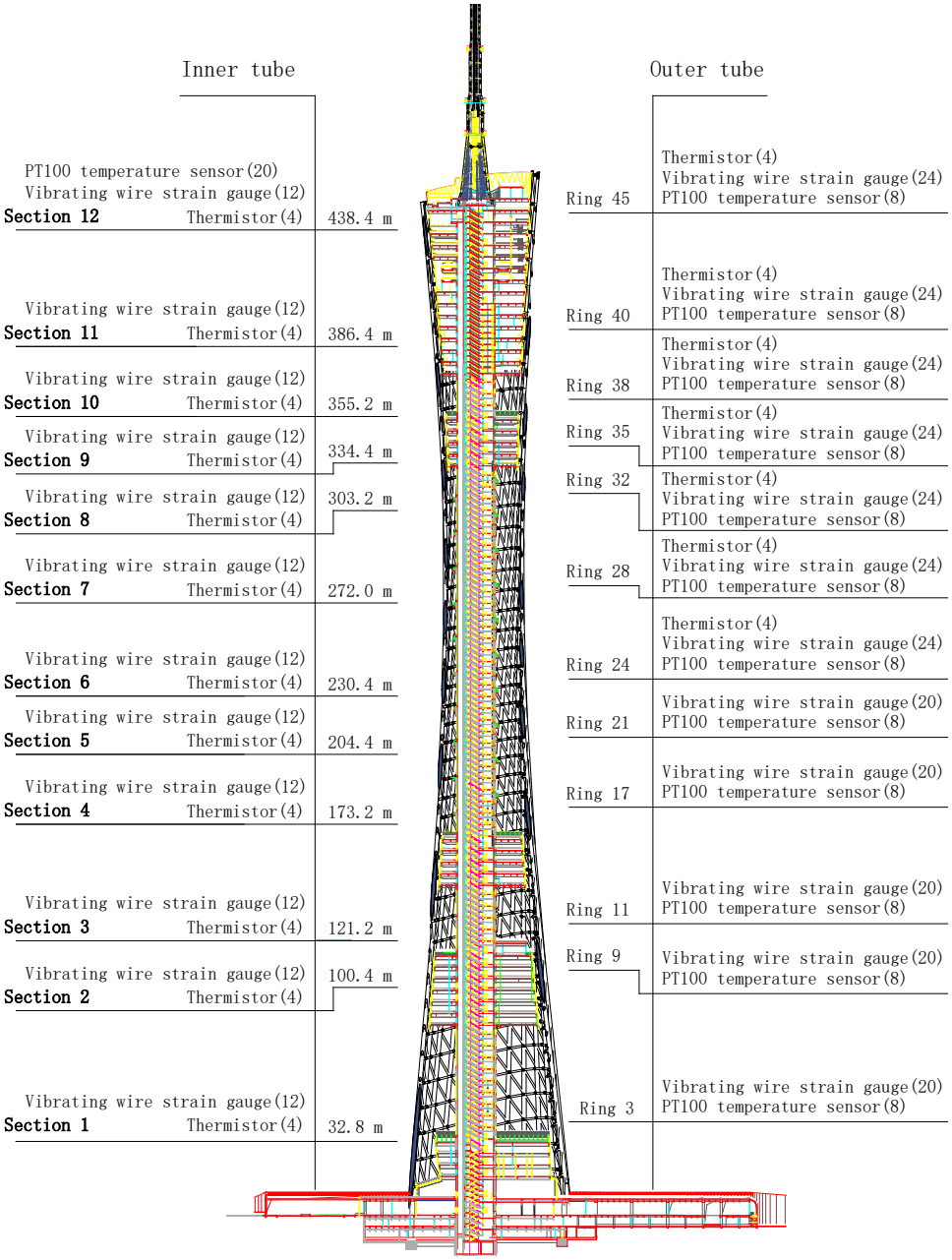

Figure 2. Deployment of temperature and strain sensors on the Canton Tower

Figures 3(a) and 3(b) show the layout of the sensors in Sections 3 and 12, respectively.

Section 12 has a functional floor enclosed by the curtain wall, whereas Section 3 has no functional floors. The plan locations of the CFT columns in the two sections vary because the columns are inclined in the vertical direction. In the inner tube, Points 1 to 4 are each embedded with three Geokon 4200 vibrating wire strain gauges [24] and one thermistor in the middle of the concrete core wall. Each vibrating wire incorporates a thermistor such that both strain and temperature at the point are measured. In the outer tube, Points A to D of each section were installed with five Geokon 4000 vibrating wire strain gauges [25] (denoted as "1" to "5") and two PT100 temperature sensors (denoted as "6" and "7"). From Sections 6 to 12, one Geokon 4200 vibrating wire was embedded in the concrete of the CFT column (denoted as "0"), which was located at one third of the radius from the column surface. The vibrating wire measures both strain and temperature at the point of the CFT column. The thermistor sensor has an accuracy of 0.2°C at the operational range of −80 ~120°C. The PT100 type thermometer has a measurement range of −20°C ~100°C with the accuracy of 0.1°C.

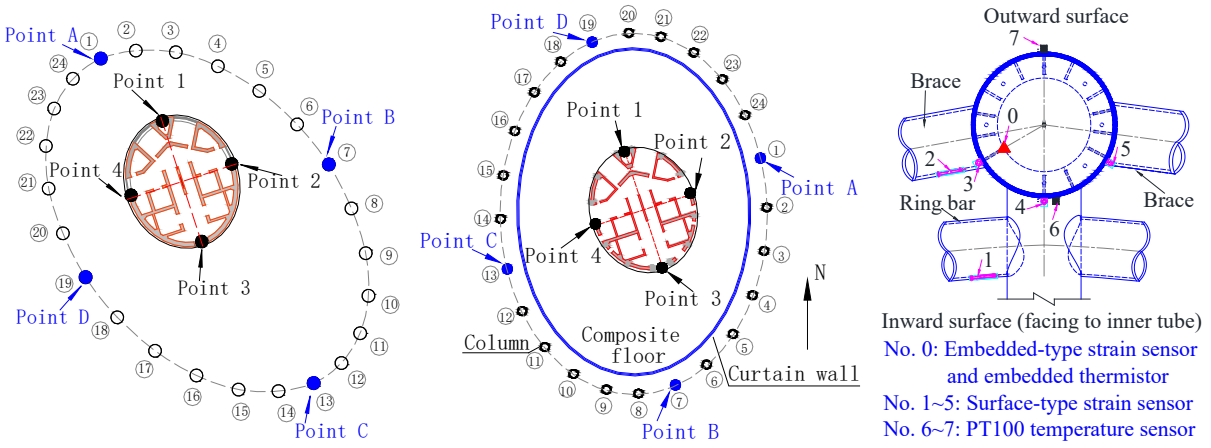

(a) (b) (c)

Figure 3. Layout of sensors on the monitoring sections: (a) Section 3, (b) Section 12, and (c) plan view of the CFT

3. TEMPERATURE MEASUREMENT DATA

The temperature data of the 12 monitoring sections were acquired, transmitted, and stored automatically by the SHM system.

3.1. Annual temperature variation

Figure 4 shows the daily maximum and minimum ground ambient air temperature data from 2008 to 2014. The measured temperature at Point 4 of Sections 3 and 9 during the period is shown in Figure 5. The period covers the construction (from January 2008 to August 2010) and service (August 2010 onward) stages of the structure. A small number of data are missed in several instances mainly because of the shutdown of the acquisition system.

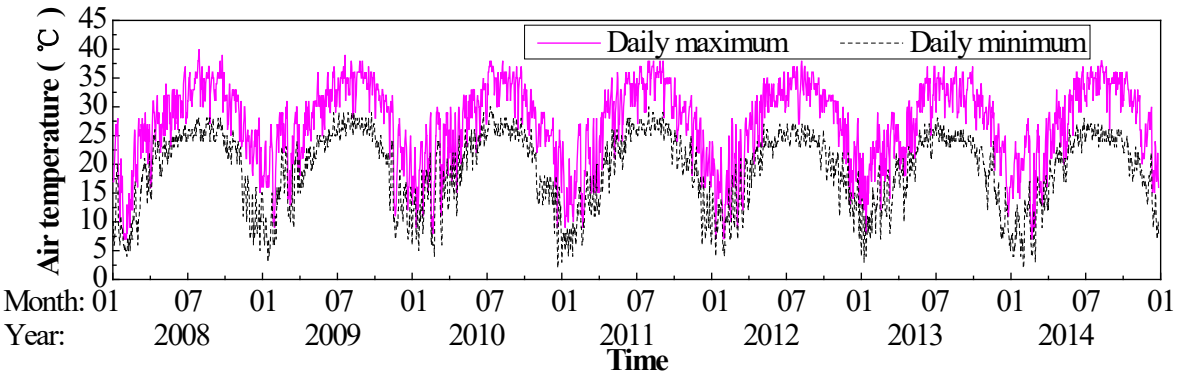

Figure 4. Daily maximum and minimum ground air temperatures from 2008 to 2014

The measured temperature data have a similar variation pattern in each year, with high temperature in the summer and low temperature in the winter for both sections. The inner wall at Section 3 is exposed to ambient air and solar radiation, whereas that at Section 9 has been enclosed by the curtain wall since early 2009. Therefore, the temperature fluctuation at Section 9 is smaller than that at Section 3 from then on (Figure 5). For example, in 2014, the minimum and maximum temperatures of Point 4 at Section 9 were 11.0 and 29.1 °C, respectively, whereas those of Point 4 at Section 3 were 8.2 and 32.5 °C, respectively.

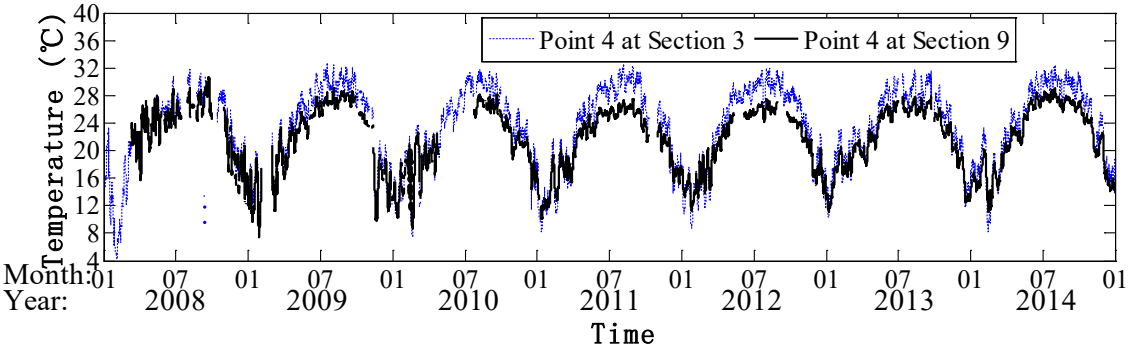

Figure 5. Measured temperature of the inner wall from 2008 to 2014

All temperature sensors on the outer tube started to collect data from August 2010. Figure 6 illustrates the measured temperature of CFT (Point C) at Section 9. The overall variation pattern of the internal concrete temperature is similar to that of the steel surface. However, the temperature variation range inside the concrete is less than that of the steel surface because concrete has low heat conductivity. In summary, the structural temperature in 2014 ranged from 2.5 °C to 29.2 °C for the concrete and from 3.1 °C to 34.8 °C for the steel surface.

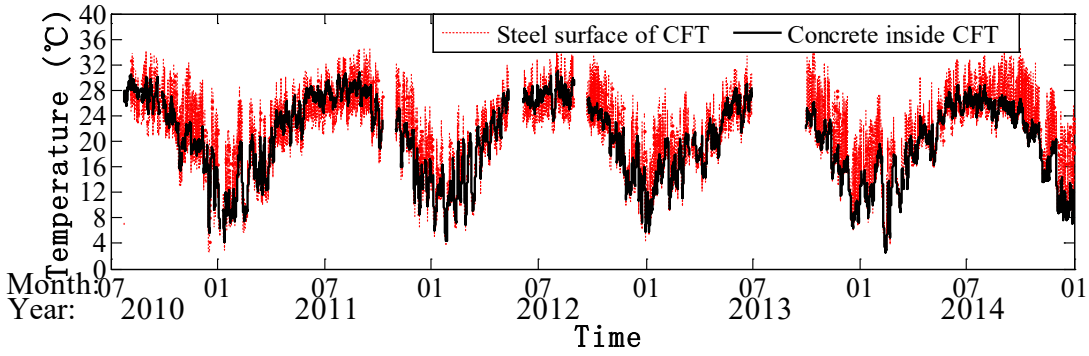

Figure 6. Measured temperature of CFT (Point C) at Section 9

3.2. Daily temperature variation

Figure 7 shows the temperature of the inner wall (Point 4) and the exterior surface of the CFT column (Point C) at Sections 3 and 9 on two successive sunny days in the summer and winter. The ambient temperature and the CFT surface temperature were observed to have a well-correlated variation cycle on the two days, although different components reach the maximum temperature at different time instants. The daily temperature fluctuation of the inner wall (Point 4) is small because the sensors are installed inside the inner wall. In particular, Point 4 of Section 9 almost has a constant temperature as the section is enclosed by the curtain wall.

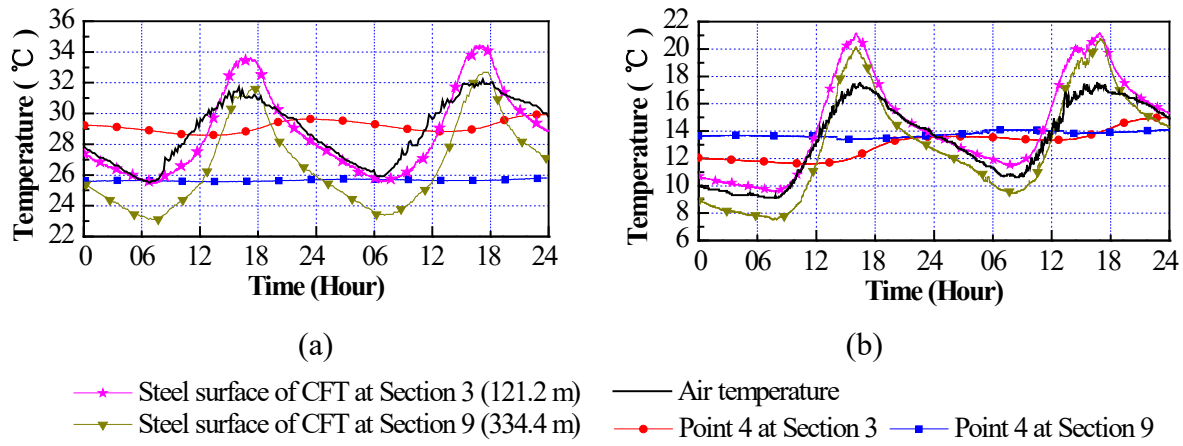

Figure 7. Temperature of the inner wall (Point 4) and outer column (Point C): (a) on 24 and 25 August 2012 and (b) on 9 and 10 January 2012

As for the steel surface of the CFT column (Point C) at Section 3 (at 121.2 m), the temperature of the steel surface has only a one-hour delay in comparison with the ambient temperature, and the daily variations are approximately 8.5 °C in the summer and 11.6 °C in the winter, which are higher than the variations of air temperature (6.0 °C in the summer and 8.0 °C in the winter). The temperature of the steel surface of Point C at Section 9 (at 334.4 m) is also lower than that at Section 3 by approximately 2 °C. The lowest temperature of the CFT surface at Section 9 is also lower than that of the ground air temperature possibly because air temperature varies with respect to the elevation, which will be investigated in the subsequent section.

3.3. Ambient air temperature

Previous studies have shown that ambient air temperature is associated with altitude and relative air humidity. For example, under normal atmospheric condition, the average air temperature decreases by 6.5 °C as the altitude increases by 1,000 m [26], and this value may be affected by the moisture content of the air.

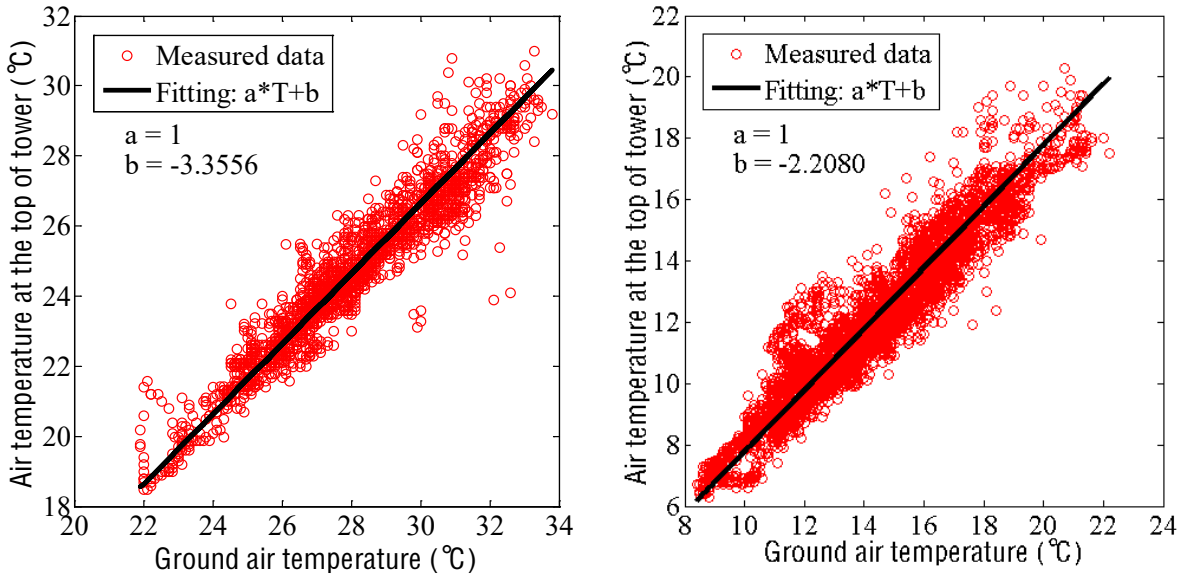

Figure 8. Relationship between the ground air temperature and the air temperature at the top of the tower: (a) September 2013 and (b) December 2014

Figure 8 shows the ground air temperature with respect to the air temperature at the top of the tower in summer and winter. The ground air temperature is higher than the air temperature at the top of the tower in both seasons. The two quantities show a good linear correlation, with correlation coefficients of 0.9563 in the summer and 0.9483 in the winter. The linear analytical function between these two quantities is expressed as $T_{tw} = a \cdot T_{gr} + b$, where T_{tw} and T_{gr} represent the air temperature at the tower top and ground, respectively, b is the intercept, and a is the slope factor. For simplicity, a is set to 1. With least squares fitting, the intercepts are obtained as $b = -3.3556$ in the summer and $b = -2.2080$ in the winter, indicating that the air temperature at the tower top is lower than the air temperature near the ground by approximately 3.4 °C in the summer and 2.2 °C in the winter. The intercepts in the summer and winter are different because of the difference in air humidity. The average temperature decrease rate is 2.8 °C/417 m = 6.7 °C/km, similar to the 6.5 °C/km rate reported by Jacobson [26].

4. TEMPERATURE DISTRIBUTION OF THE CANTON TOWER

Previous studies [9-11] show that the temperature difference between the inner and outer tubes and the temperature difference between different facades of the inner tube and outer

columns are two main temperature profiles for highrise structures. The former component will cause the inner and outer tubes to have different vertical deformations, yielding the shear forces and bending moments at the floor; whereas the latter will cause the lateral deformation of the tower. Both will be investigated in this section.

4.1. Effective temperature of the main components

The temperature distribution along the thickness of the RC core wall, as well as that over the cross section of the CFT columns, are non-uniform. Thus, the effective temperature is employed for simplicity. The effective temperature is an area-weighted average temperature of the cross-section of the structural component [27, 28]. For example, an area A consists of several subareas A_i (i = 1, 2, …, k), each of which has an average temperature $\overline{T}_i$. Then, the effective temperature of the component can be calculated as $T_e = \sum_{i=1}^{k} \frac{A_i}{A} \overline{T}_i$.

For the Canton Tower, the temperatures at Points 1, 2, 3, and 4 are considered as the effective temperature of the inner core walls facing the north, east, south, and west, respectively, because only one thermistor sensor was installed at the middle thickness of the wall at each point.

For the CFT columns, the steel surface and inside the concrete have different temperature distributions. In view of the difficulty in measuring the detailed temperature distribution of the CFT columns by only a few sensors, the temperature distribution can be obtained through a numerical heat conduction analysis. The analysis is based on the principle that the time rate of the heat flow through a body is proportional to the temperature gradient, governed by the Fourier partial differential equation [7, 29]. Since the structural temperature varies with respect to time, the heat flow is referred to as transient conduction or non-steady-state conduction. In this regard, the FE model of a typical column section at Point C of Section 8 is constructed in ANSYS [30] and is shown in Figure 9(a). The FE model consists of 400 nodes and 360 two-dimensional Plane55 elements. Plane55 has four in-plane nodes, each with a single DOF of temperature.

For transient heat conduction analysis, the thermal boundary condition should be

determined first, that is, the temperature of the exterior surface of the CFT column at different time should be available. Since two temperature sensors have been installed on the column surface (refer to Nos. 6 and 7 in Figure 3c), they provide the real temperature of the two points at different time. The temperatures of other surface points are then estimated from the two sensors. In this regard, the CFT exterior surface is divided into four regions, namely, outward surface, inward surface, and two side surfaces, according to their orientations. The temperatures of the outward and inward surfaces are respectively represented by the actual temperature measured from the two temperature sensors. The temperatures of the two side surfaces are represented by the average temperature of the two sensors.

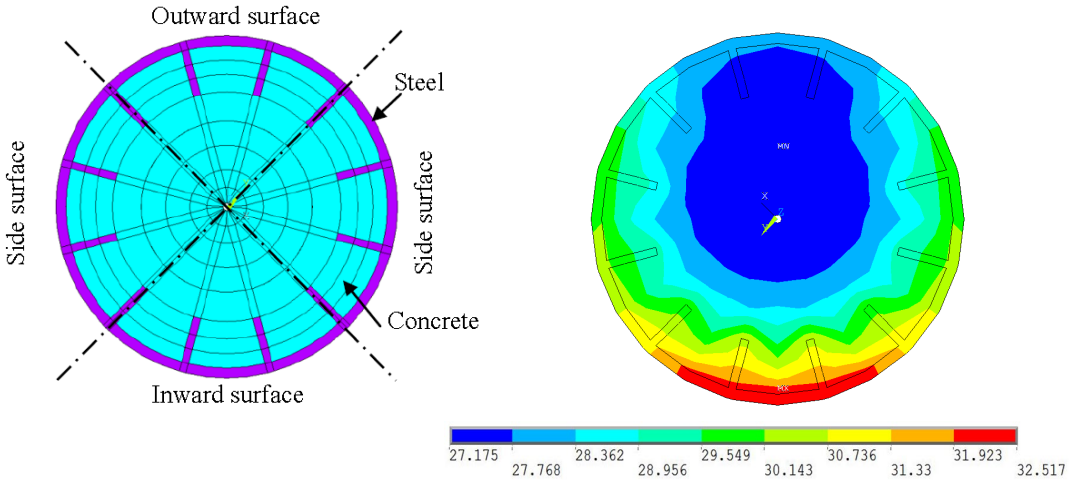

(a) (b)

Figure 9. FE model of the CFT column for heat transfer analysis: (a) CFT column section and (b) temperature contour

The main material properties used in the heat transfer analysis are summarized in Table I. With the transient heat transfer analysis in ANSYS, the temperature variation of the column at different time instants is obtained. Figure 9(b) shows the temperature contour of the section at 15:00 on 4 August 2011. The temperature is nonuniformly distributed with an approximate 5.3 °C difference between the steel surface and inside the concrete.

The simulated temperature inside the concrete is compared with the measurement counterpart (the measurement point is shown in Figure 3(c)) and shown in Figure 10. The numerical results are consistent with the field measurement, with a difference of less than 0.5 °C, which verifies the effectiveness of the heat transfer analysis.

Table I. Material parameters of the column for thermal analysis [20]

Parameters	Density (kg/m^3)	Heat capacity (J/(kg °C))	Thermal conductivity (W/(m °C))	Emissivity coefficient	Absorptivity coefficient
Steel	7,850	460	60	0.80	0.75
Concrete	2,400	925	2.71	0.88	0.65

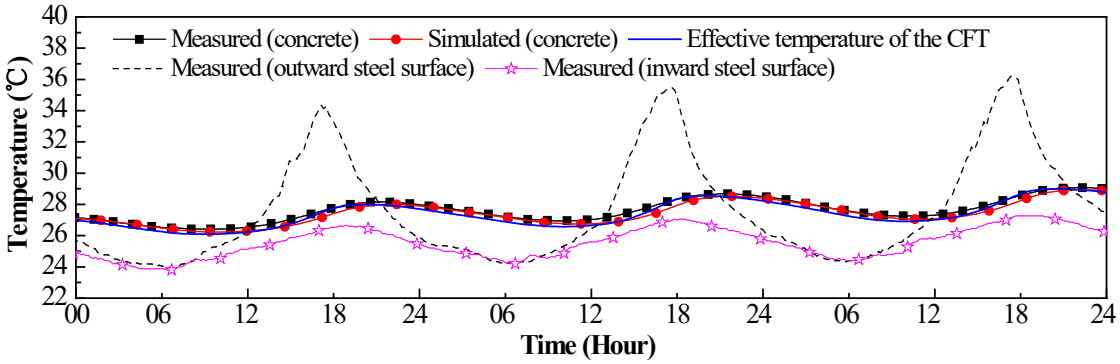

Figure 10. The simulated and measured temperatures of the CFT column at Point C of Section 8 on 2–4 August 2011

According to the simulated temperature data at each point, the effective temperature of the cross-section is calculated and plotted in Figure 10. The effective temperature of the section is close to the measured concrete temperature. Consequently, the measured temperature inside the column will be considered the effective temperature of the composite section of the column and will be employed in the subsequent analysis.

4.2. Temperature difference between the inner and outer tubes

First, we analyze the temperature difference between the CFT column and the inner core wall in the same structural facade. The effective temperature of the corresponding components previously described is employed. A positive temperature difference denotes that the CFT column has a higher temperature than the inner wall.

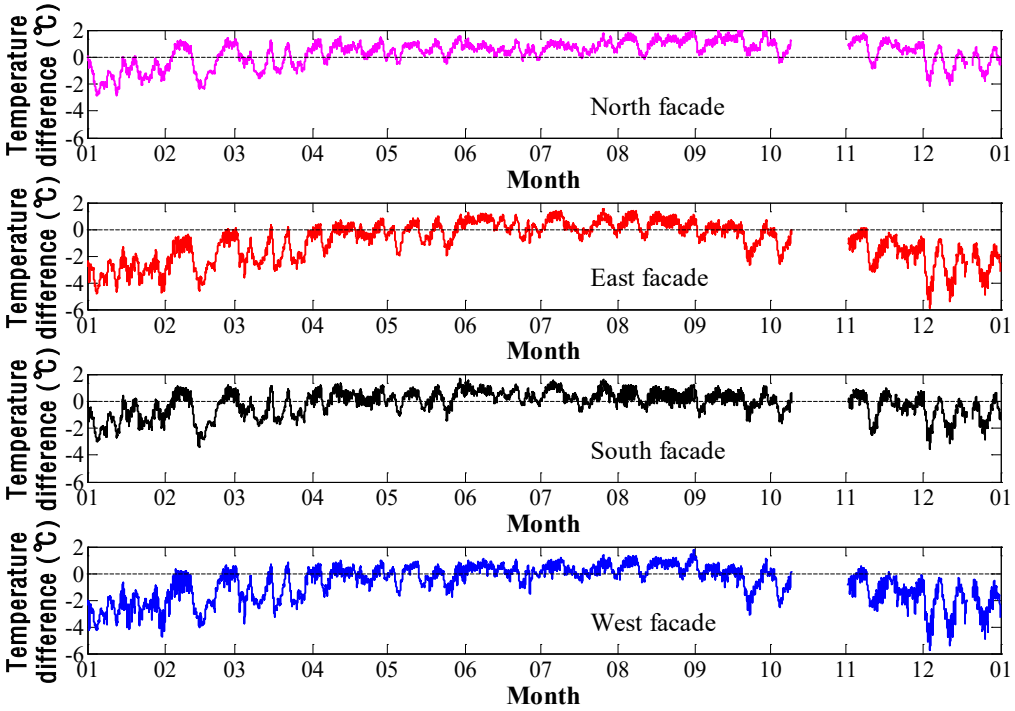

Figure 11. Temperature difference between the inner and outer tubes at Section 8 in 2011

The temperature differences at Sections 8 and 12 in the entire year of 2011 are shown in Figure 11 and Figure 12, respectively, representing two typical structural configurations. In Section 8, the inner and outer tubes are exposed to the ambient environment and are observed to have similar thermal conditions. By contrast, the inner tube of Section 12 is enclosed by the curtain wall, whereas the outer tube is exposed to the ambient environment. The results show that Section 8 has the maximum positive temperature difference of 2.0 °C in the summer and the maximum negative temperature difference of −6.0 °C in the winter. However, Section 12 has the maximum positive temperature difference of 8.1 °C in the summer and the maximum negative difference of −15.0 °C in winter, which are more significant than those in Section 8. This difference is due to the fact that the curtain wall keeps the inner tube under a stable temperature condition. In particular, the inner tube is significantly cooler in the summer and warmer in the winter than the outer CFT columns. Consequently, its lateral temperature difference is more significant than that without the curtain wall.

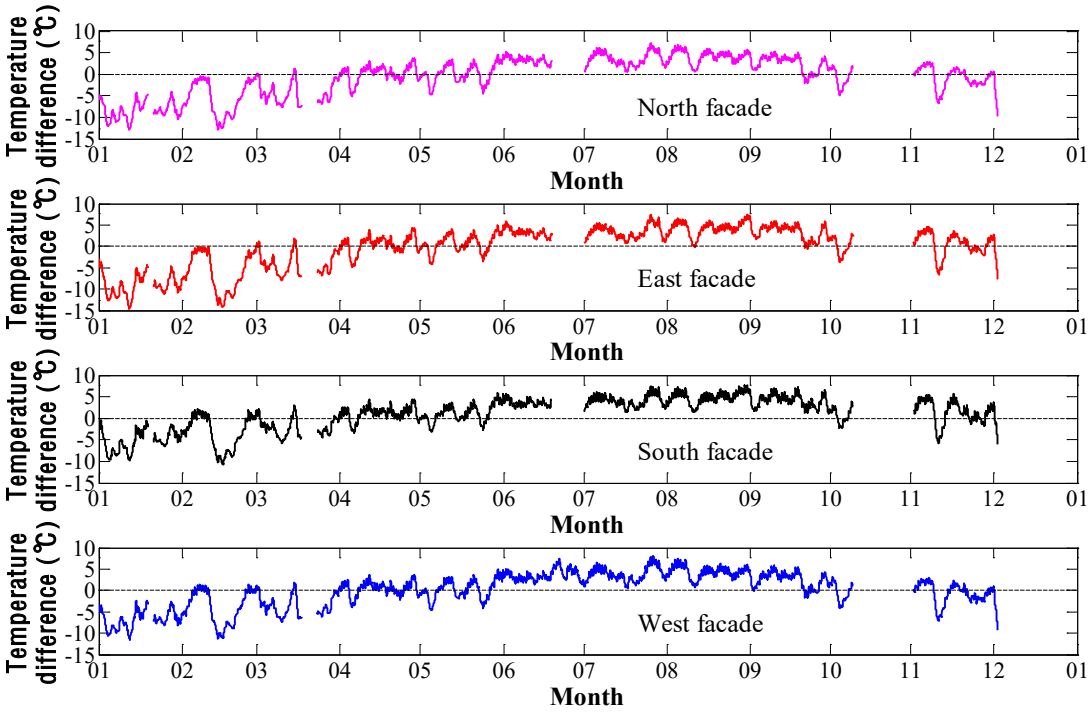

Figure 12. Temperature difference between the inner and outer tubes at Section 12 in 2011

The maximum temperature differences at Sections 1 to 12 in 2011 are listed in Table II. For Sections 1 to 5, the temperature of the CFT columns are obtained from the numerical heat transfer analysis because no temperature sensor has been installed inside these columns. The maximum positive differences of all sections occur in the summer (July and August), and the maximum negative differences of all sections occur in the winter (December and January). The orientation of the maximum difference of each section is different, which might occur at all facades, except the north. In this regard, the temperature differences of the four facades are averaged at each monitoring section to analyze the distribution of the temperature difference along the height of the structure.

Among all sections, Section 12 has the largest temperature difference (−15.0 and 8.1 °C), which is significantly larger than that at Section 11 (−9.2 and 3.2 °C), although the inner tube of Sections 11 and 12 are enclosed by the curtain wall. This difference may be due to the fact that the functional floors of Sections 9 to 12 have different functions and their indoor temperatures are set to be different during the operation. This phenomenon is shown in Figure 13, which reveals that the temperatures of the inner tubes (Point 3) at Sections 11 and 12 were similar in 2009 during the construction stage, but were quite different in the middle

of 2010 when the service stage started.

Table II. Maximum temperature difference between the inner and outer tubes in 2011

Monitoring section	Maximum positive value (°C)	Orientation	Time (month)	Maximum negative value (°C)	Orientation	Time (month)
Section 1	5.0	West facade	August	−9.0	West facade	December
Section 2	3.1	West facade	August	−5.0	West facade	December
Section 3	1.0	West facade	August	−2.1	West facade	December
Section 4	0.9	West facade	August	−2.6	West facade	December
Section 5	0.8	South facade	August	−2.5	East facade	December
Section 6	1.0	South facade	August	−2.8	East facade	December
Section 7	1.9	West facade	August	−5.3	West facade	December
Section 8	2.0	West facade	August	−6.0	East facade	December
Section 9	4.0	East facade	August	−7.7	West facade	January
Section 10	4.5	West facade	August	−9.7	West facade	January
Section 11	3.2	South facade	August	−9.2	South facade	December
Section 12	8.1	West facade	July	−15.0	East facade	January

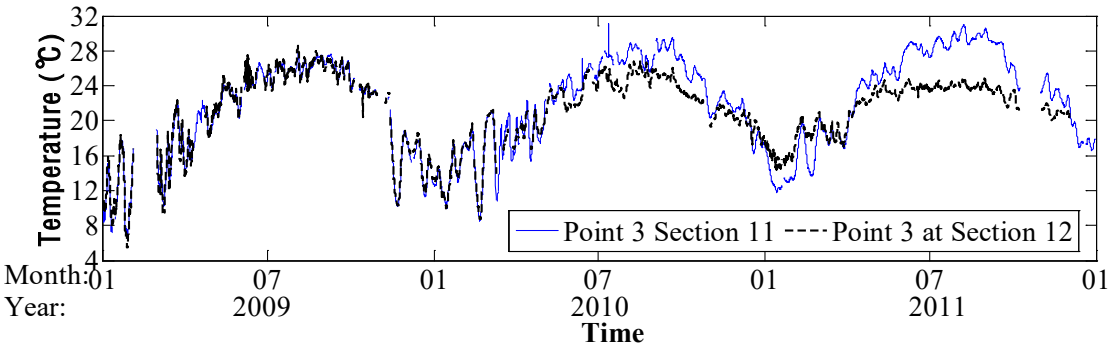

Figure 13. Temperature of the inner tube (Point 3) at Sections 11 and 12

Figure 14 shows the distribution of the inner and outer temperature difference along the height, in which the star marks are respectively the maximum temperature difference in the years of 2010 to 2014. In general, for Sections 3 to 8 without functional floors, the temperature difference between the inner and outer tubes is relatively small in both seasons. For the other sections with functional floors, the temperature difference between the inner and outer tubes is significant and similar, except for Section 12, as previously explained.

Based on the previously presented observations, the envelope of the temperature difference with respect to the height of the structure can be categorized into three groups, as

the solid lines shown in Figure 14: (i) the largest temperature difference, $T_a^{+,-}$ for Section 12 and the segment between Sections 11 and 12; (ii) $T_b^{+,-}$ for Sections 1 to 3 and Sections 9 to 11 with functional floors; and (iii) $T_c^{+,-}$ for Sections 3 to 9 without functional floors. The superscripts "+" and "–" denote the positive and negative temperature differences, respectively. In this study, T_a^+ = 8.0 °C, T_b^+ = 5.1 °C, and T_c^+ = 3.0 °C in the summer, whereas T_a^- = −15.0 °C, T_b^- = −9.7 °C , and T_c^- = −6.0 °C in the winter.

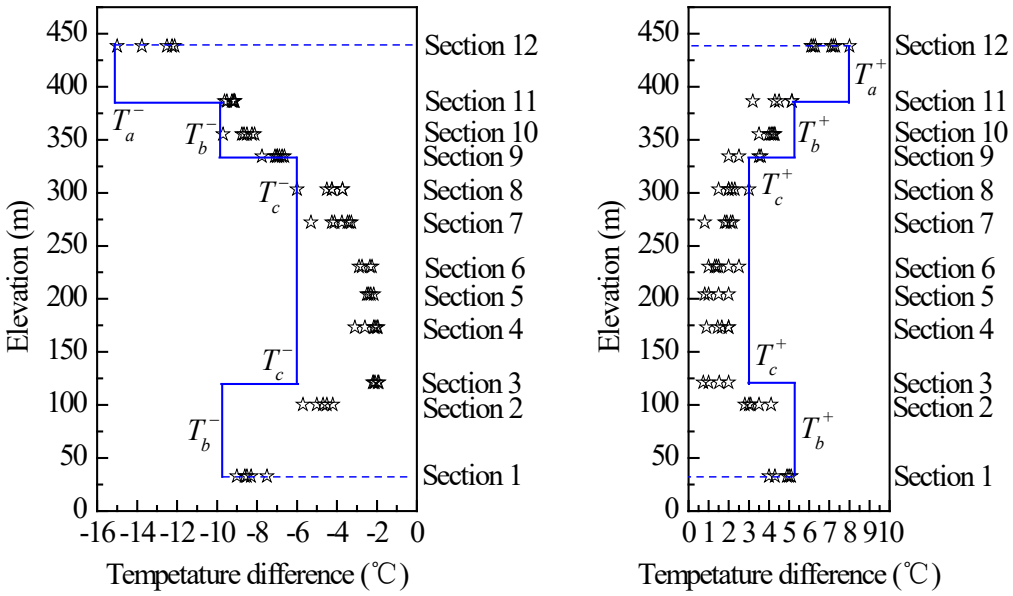

(a) (b)

Figure 14. Distribution of temperature differences along the height of the structure: (a) in the winter and (b) in the summer

4.3. Temperature difference between the different faces of the structure

4.3.1. Inner concrete wall

In this section, the temperature difference of the inner walls among the different facades will be investigated. We define $\Delta T_{ij} = T_i - T_j$, where T_i and T_j (i, j = 1, 2, 3, 4) represent the temperatures at Points 1 to 4. The locations of these measured points are shown in Figure 3.

Figure 15 illustrates the temperature difference between different facades of Sections 8 and 12 in 2014. The temperature difference fluctuates slightly in the range of −2.0 to 1.5 °C in Section 12, indicating that the inner walls with functional floors enclosed by the curtain walls

have a uniform temperature distribution over different facades. Therefore, their temperature difference is negligible.

The temperature difference at Section 8 is almost positive during the entire year, indicating that the temperature of the north facade is the lowest over the year, as expected. Winter has the largest difference of approximately 4.5 °C. Several areas of the exterior surface of the wall are found in the shadow of the CFT columns, thus receiving only a portion of solar radiation. Therefore, the temperature difference between the facades of Section 8 remains at a low level and is slightly higher than that of Section 12.

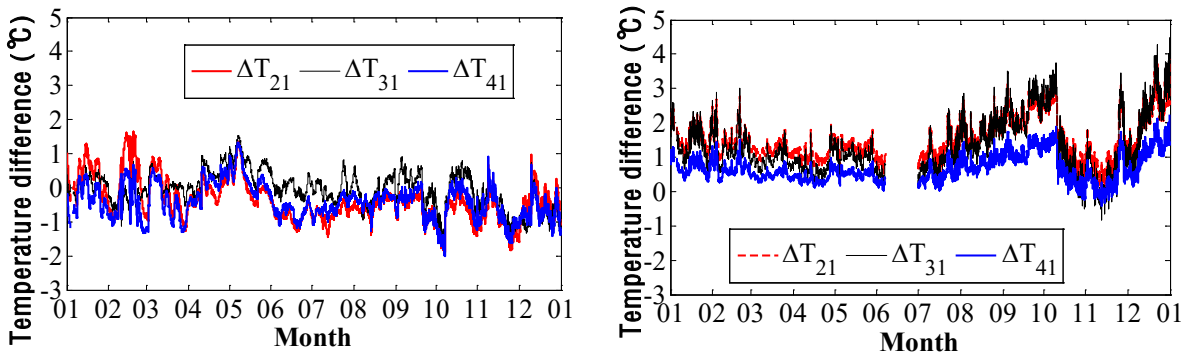

Figure 15. Temperature difference between different facades of the inner tube in 2014: (a) Section 12 and (b) Section 8

4.3.2. Outer CFT columns

For the outer CFT columns, we define $\Delta T_{mn} = T_m - T_n$, where T_m and T_n (m, n = N, E, S, W) represent the temperatures of the monitoring columns on the north, east, south, and west facades. The outer CFT columns receive different levels of solar radiation, causing the temperature difference on different facades. Figure 16 shows the temperature difference between the columns on the south and north facades at Sections 8 and 12 in 2011. For each CFT column, the effective temperature of the column section is used. A positive temperature difference denotes that the south facade has a higher temperature than the north facade. The temperature of the south facade is higher than that of the north facade throughout the year, as expected. Winter also has a larger temperature difference than summer, with a maximum value of 6.0 °C.

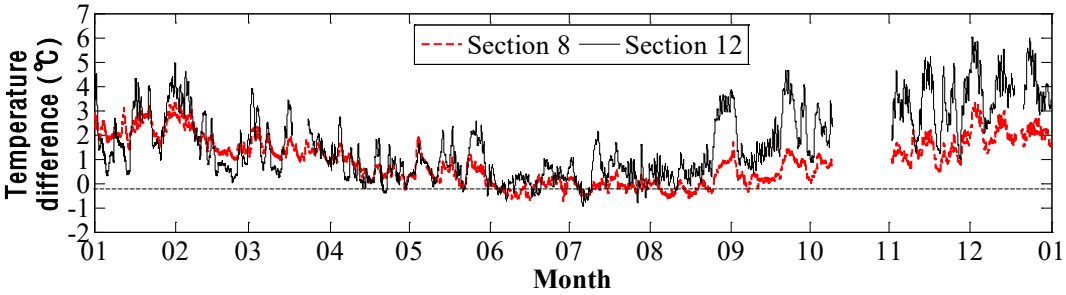

Figure 16. Difference between the temperature of the south column and that of the north in 2011

As the outer columns are inclined in the vertical direction, the monitoring points at different sections rotate in the plan view. The temperature difference of all monitoring points in typical summer and winter days is illustrated in Figure 17, where the alphanumeric code represents the CFT column, for example, “12A” denotes Point A at Section 12. The lowest temperature of the columns is selected as the reference, and the temperature difference is shown in the figure.

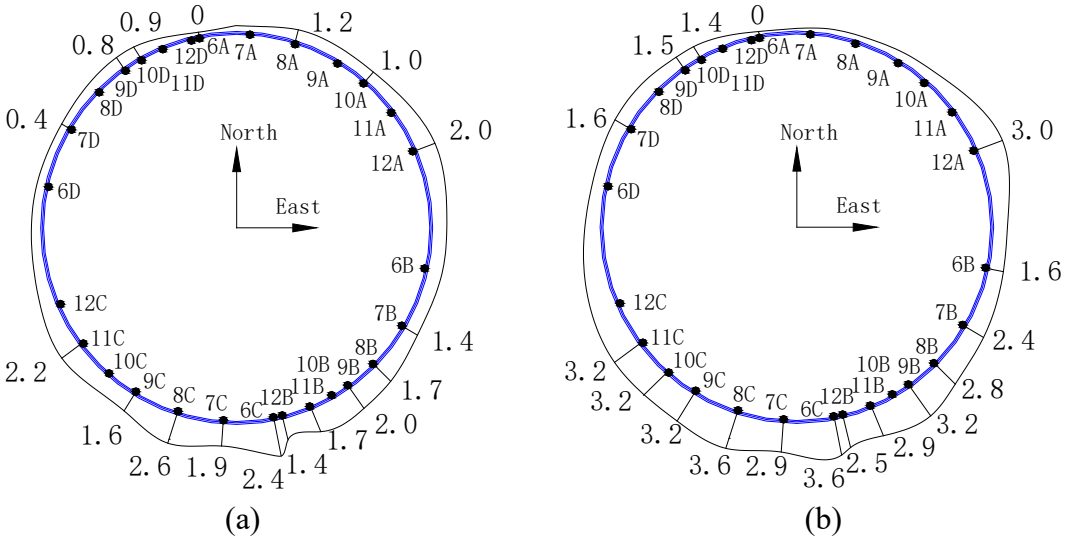

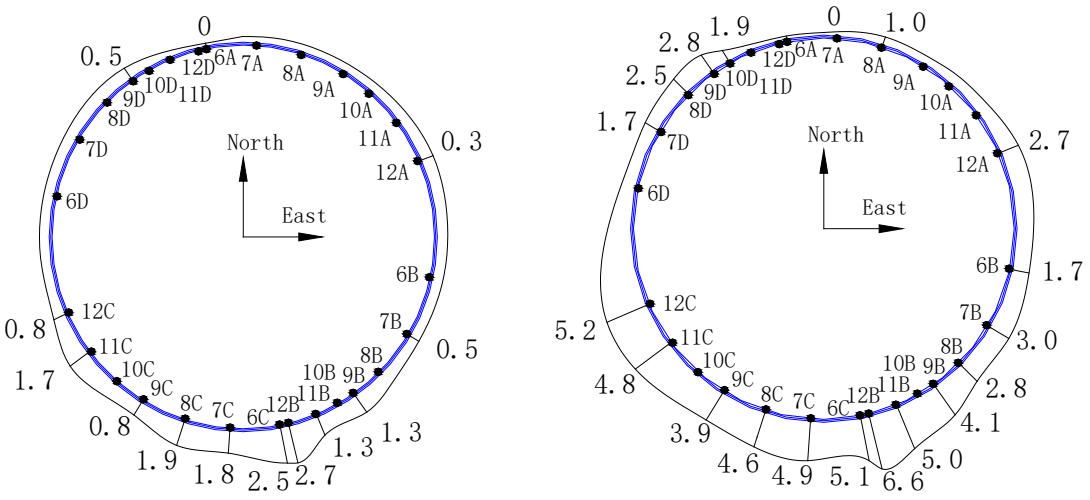

Figure 17. Temperature difference profile of the outer tube (unit: °C): (a) 07:00 on 21 June 2012, (b) 19:00 on 21 June 2012, (c) 08:00 on 22 December 2011, and (d) 18:00 on 22 December 2011

These two typical days are the summer solstice (on 21 June 2012) and the winter solstice (on 22 December 2011), which represent the longest and shortest days of the year in the northern hemisphere, respectively. As expected, the south facade has the highest temperature and the north facade has the lowest. The temperature difference between different facades of the outer tube, which is less than 2.5 °C in the summer and winter, is relatively uniform before sunrise. The difference increases after sunrise and reaches 3.6 °C in the summer and 6.6 °C in the winter. This finding implies that the difference in the winter is more significant than that in the summer. This implication is attributed to the fact that the Canton Tower is located on the Tropic of Cancer. The sun rises from the east and appears highest in the sky in the summer solstice. Thus, the temperature difference between the north and south is small. From summer to winter, the sun moves to the southern hemisphere gradually. In the winter solstice, the south facade receives significantly more solar radiation than the north facade. Thus, the temperature difference between the south and north facades is significant.

Figure 18 shows the envelope curve of the maximum temperature difference of the outer tube from 2010 to 2014. The figure shows that the columns in the south have the highest temperature, followed by those in the west, east, and north.

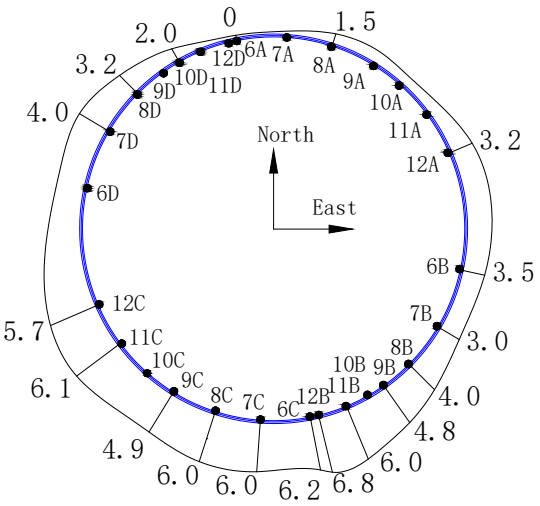

Figure 18. Maximum temperature difference of the outer tube (unit: °C)

5. TEMPERATURE-INDUCED RESPONSES FROM FIELD MONITORING

5.1. Temperature-induced displacement

A GPS was installed to monitor the horizontal displacement of the Canton Tower. The measured horizontal displacement track at the top of the tower on four sunny days in different seasons is illustrated in Figure 19. The dates are 14 April 2013, 11 August 2013, 12 October 2013, and 1 January 2014, representing spring, summer, autumn, and winter, respectively. These days all had a significant daily air temperature variation of more than 10 °C. The wind speed of these days was no more than 3.5 m/s. Therefore the displacement was mainly induced by the thermal load. The positions of the daily movement track shown in the figure were the averaged data for every half-hour period.

On 1 January 2014, the tower moved relatively slow before sunrise, moved to the northwest after sunrise, and reached its westernmost position at approximately 12:00. This movement is attributed to the fact that the sun rises from the southeast direction in the winter, causing the members in the southeast to have higher temperature than those in the shaded facade. Consequently, the structure bent away from the sun. For the same reason, the temperature of the members in the southwest increased when the sun moved to the southwest in the afternoon, causing the tower to move toward the northeast and reaching its

northernmost position at approximately 16:00. After sunset, the temperature difference between the tower members decreased. Therefore, the tower moved back gradually from the north to the south and finally returned to its initial point (at 24:00). The peak-to-peak motion throughout the day was 15.7 cm in the east–west direction and 15.5 cm in the south–north direction, and the maximum displacement was approximately 20 cm.

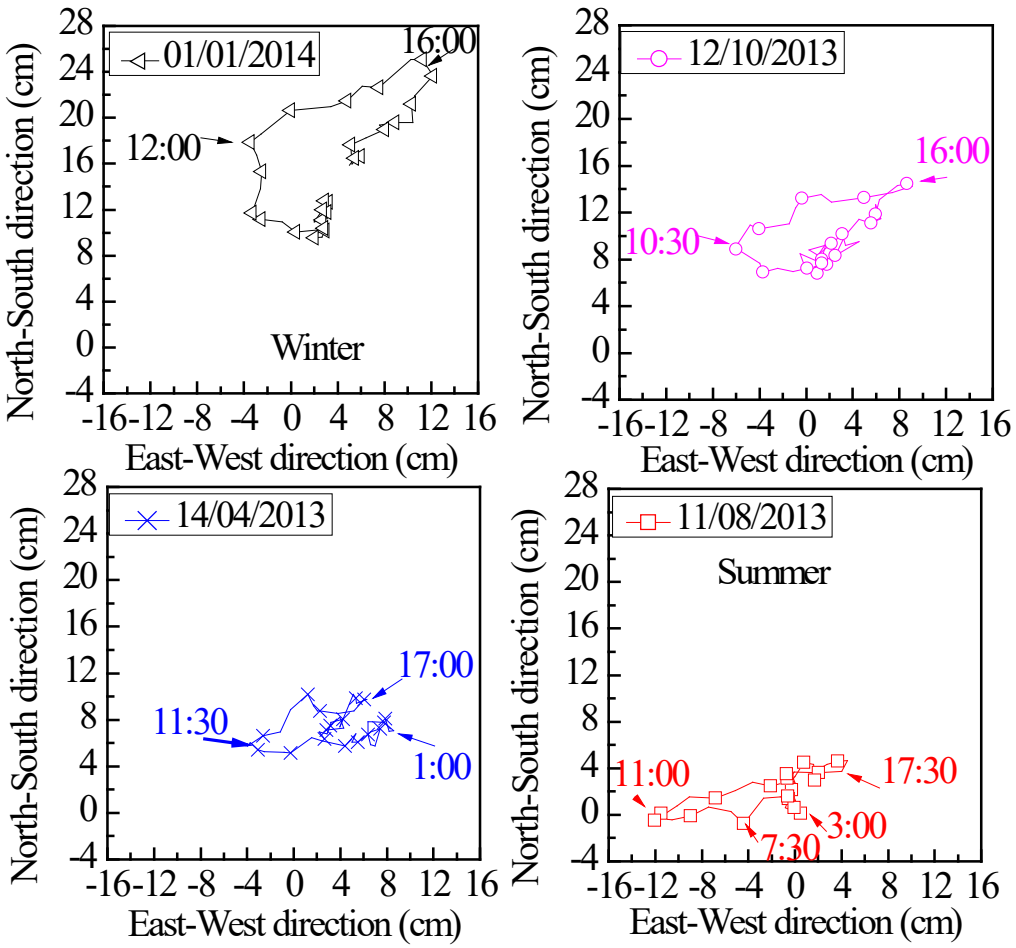

Figure 19. Measured temperature-induced horizontal displacement track at the tower top on four sunny days in different seasons

The daily movement of the tower top on these four days exhibited a similar pattern, which is in the clockwise direction. The tower top also moved toward the northeast by approximately 15 cm (between the centroids of the tracks) from summer to winter because the south facade receives more solar radiation than the north facade in the winter. Therefore, their temperature difference is significant and the tower bends toward the north.

The daily horizontal displacement in the east–west direction on sunny days in different

seasons was approximately similar (12 cm to 16 cm). However, the daily horizontal displacement in the south–north direction in the winter (15 cm) was significantly larger than that in the summer (5 cm), as shown in Figure 20, because winter caused a significant temperature difference between the south and north facades.

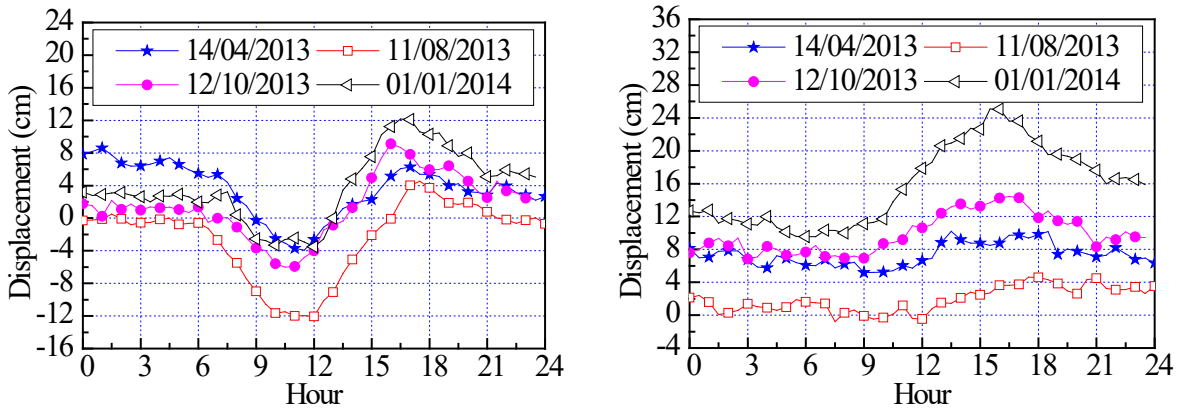

(a) East–west direction (b) South–north direction

Figure 20. Measured horizontal displacement at the tower top on four sunny days in different seasons: (a) east–west direction and (b) south–north direction

5.2. Temperature-induced stress

For an axially loaded member composed of a single material, stress σ is calculated by using the following equation:

$$\sigma = E\left(\varepsilon - \alpha_T \Delta T\right), \tag{1}$$

where ε is the measured total strain, E is the modulus of elasticity for the material, and α_T is the thermal coefficient of the linear expansion of the material. For the RC core wall of the inner tube, the stress is calculated based on the material properties of concrete. Although the stress of the wall is basically observed in three dimensions, only the vertical stress is investigated in this study. For the outer CFT columns made of steel and concrete, their moduli are quite different. Thus, the equivalent stress of the columns can be calculated as follows:

$$\bar{\sigma} = \frac{A_c E_c \left(\varepsilon_c - \alpha_c \Delta T_c\right) + A_s E_s \left(\varepsilon_s - \alpha_s \Delta T_s\right)}{A_c + A_s}, \tag{2}$$

where subscripts "*c*" and "*s*" denote the properties of concrete and steel, respectively.

The vertical ordinate axis of Figure 21 denotes the total stress, which includes self-weight stress. The strain gauges were installed on the tower during the construction, and zero stress was the moment when the component construction was completed. Therefore, these sensors were able to track the complete historic change in the parameters from the onset of construction, thus achieving life cycle monitoring of the structure. This integrated monitoring system enables the measurement of cumulative strain, which is necessary for evaluating the real safety index of the structural components and the effect of extreme events (such as earthquake, strong winds, fire, and man-made disasters) on the structural performance.

The measured vertical stress of the inner tube increased (compression decreased) as temperature increased from winter to summer (Figure 21(a)). This finding indicates tension in the inner tube as the structural temperature increased from winter to summer. Then, the equivalent stress of the outer CFT column at Section 8 is calculated from the measured stresses of the steel surface and concrete of the column and is shown in Figure 21(b). The stresses of the CFT columns on the northeast facade increased, whereas those on the southwest facade decreased. This is because the temperature of the outer CFT columns on the south facade increased more than that of the inner wall from winter to summer, which caused the outer columns to have a larger expansion deformation in the vertical direction than the inner wall. Such a nonuniform expansion between the inner and outer tubes resulted in tensile stress in the inner core and compressive stress in the outer columns.

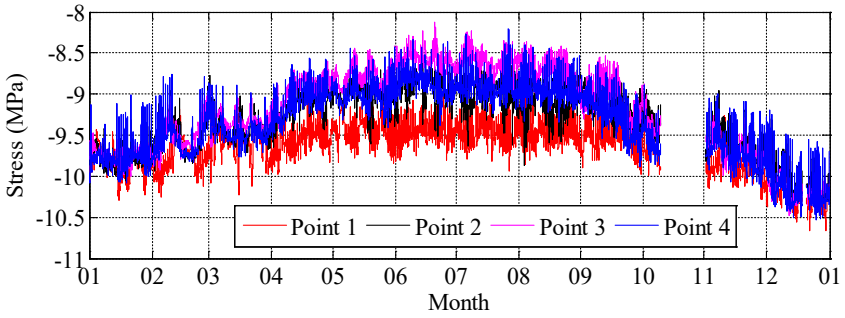

(a)

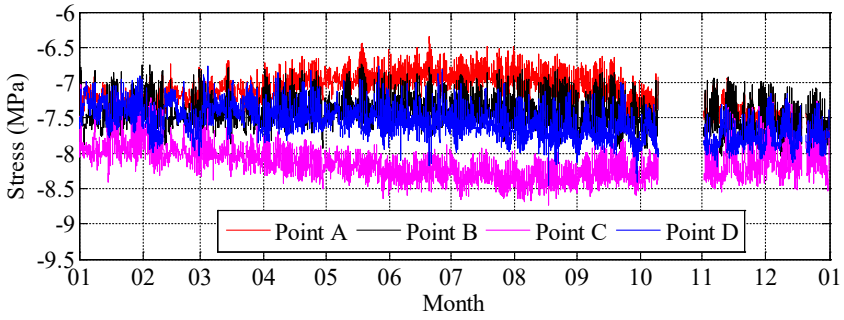

(b)

Figure 21. Measured stress at Section 8 in 2011: (a) inner tube and (b) outer tube

6. TEMPERATURE-INDUCED RESPONSES FROM THE NUMERICAL SIMULATION

Several temperature loading cases with the measured temperature distribution of the structural components are applied to the SAP2000 FE model of the tower (Figure 1(d)) to verify the measured temperature-induced displacement of the tower top. The temperature distribution of the entire structure at 03:00 on 11 August 2013 is selected as the reference state (Case 0), in which the temperature difference among the structural components is small. The temperature distributions at 11:00 and 17:30 on the same day with significant temperature differences are selected as Cases 1 and 2, respectively. Three cases in the winter, namely, 04:00 (Case 3), 12:00 (Case 4), and 16:00 (Case 5) on 1 January 2014 are also analyzed to determine the temperature effects in different seasons.

6.1. Temperature model

Although the temperature distribution of several points of the structure has been obtained, obtaining the detailed temperature distribution of all components of the entire structure is difficult. For this reason, the global temperature distribution of the FE model is simplified as follows:

(i). The inner and outer tubes are divided into four regions, namely, north, east, south, and west facades. The components on the same facade are assumed to have similar temperatures at one time instant.

(ii). The temperature of the floor slab is assumed to be equal to the mean temperature of the inner tube because the floor slabs are enclosed by the curtain wall.

(iii). The temperature difference between the inner and outer tubes is calculated by using the simplified model with respect to the height of the structure (see Figure 14). This difference is simplified to be the difference between the mean temperature of the inner wall and the mean temperature of four outer columns (see Table III).

(iv). The inner tube with functional floors has a uniform temperature distribution over different facades. The inner tube without functional floors has a uniform temperature distribution in the summer, whereas its south and west facades have higher temperature than the north facade in the winter, as listed in Table III.

(v). In the outer tube, the east, south, and west facades have higher temperatures than the north facade in the winter and summer.

Table III. Simplified temperature differences in Cases 0 to 5

Case	Temperature difference (°C)								
	T_a^+	T_b^+	T_c^+	ΔT_{21}	ΔT_{31}	ΔT_{41}	ΔT_{EN}	ΔT_{SN}	ΔT_{WN}
Case 0	4.4	3.7	0.9	0	0	0	0.4	0.3	1.3
Case 1	4.9	4.1	0.6	0	0	0	3.0	1.4	0.6
Case 2	4.7	4.0	0.2	0	0	0	0.8	1.2	2.0
	T_a^-	T_b^-	T_c^-	ΔT_{21}	ΔT_{31}	ΔT_{41}	ΔT_{EN}	ΔT_{SN}	ΔT_{WN}
Case 3	−9.6	−7.1	0.1	0.6	2.5	1.3	1.7	3.8	1.9
Case 4	−8.9	−7.1	0.1	3.2	3.9	1.9	3.7	5.1	2.4
Case 5	−8.6	−6.1	0.6	1.4	4.1	3.0	2.0	6.7	5.4

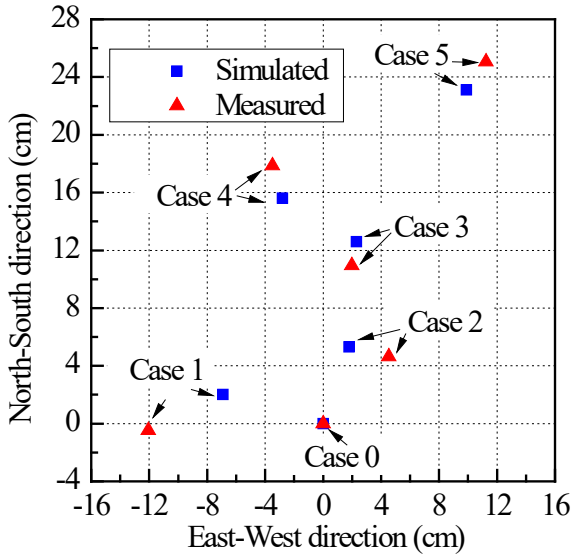

Figure 22. Simulated and measured horizontal positions of the tower top

In all cases, the temperature data are inputted into the FE model. The position of the entire structure in Case 0 is regarded as the initial state. Then, the changes of other cases to Case 0 are calculated and regarded as the thermal-induced responses. Figure 22 shows the calculated horizontal displacement of the tower top (465 m) in all cases, as compared with the field measurement. The calculated horizontal displacement under the simplified temperature loads is consistent with the field measurement, which revealed that the temperature-induced displacement in the winter is larger than that in the summer in the east–west and south–north directions. The tower top also moved toward the northeast direction from summer to winter. The differences between the calculated and measured results are less than 2.5 cm in most of the cases. Therefore, the simplified temperature model is effective in obtaining the thermal-induced responses of the structure.

6.2. Temperature-induced displacement

Figure 23 plots the simulated temperature-induced horizontal and vertical displacement profiles of the tower along the height in Case 5, when the tower had the maximum horizontal displacement relative to the reference state. The horizontal displacement exhibits the bending mode, which is different from the bending–shear mode of a typical frame–wall structure. This is because the floor girders are pin-connected to the outer CFT columns through bolts such that the outer columns rotate freely to release the bending moment of the joints between the inner and outer tubes. Consequently, less restraint acts on the deformation between the inner tube and the outer CFT column. Different facades of the same height also had quite consistent horizontal displacement induced by the temperature load.

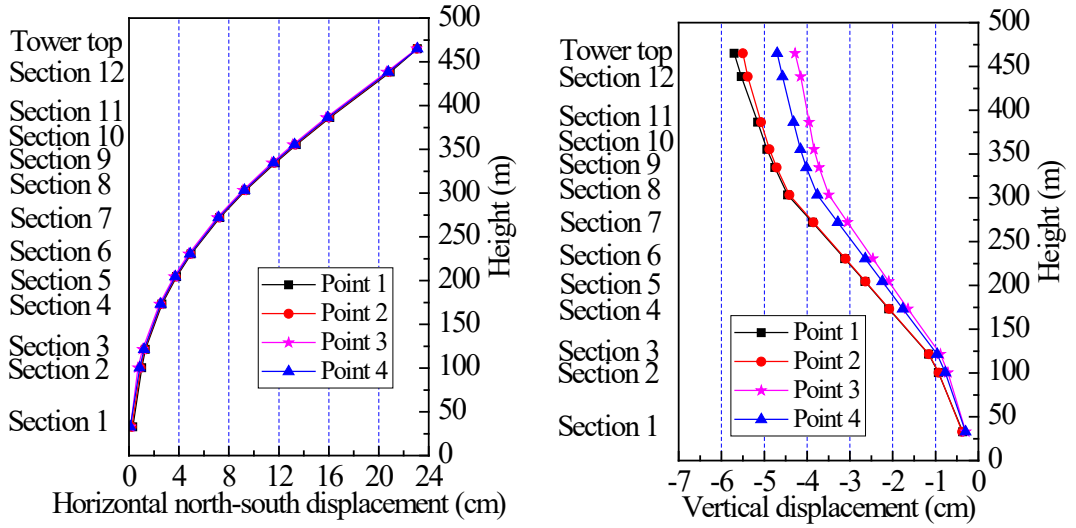

(a)

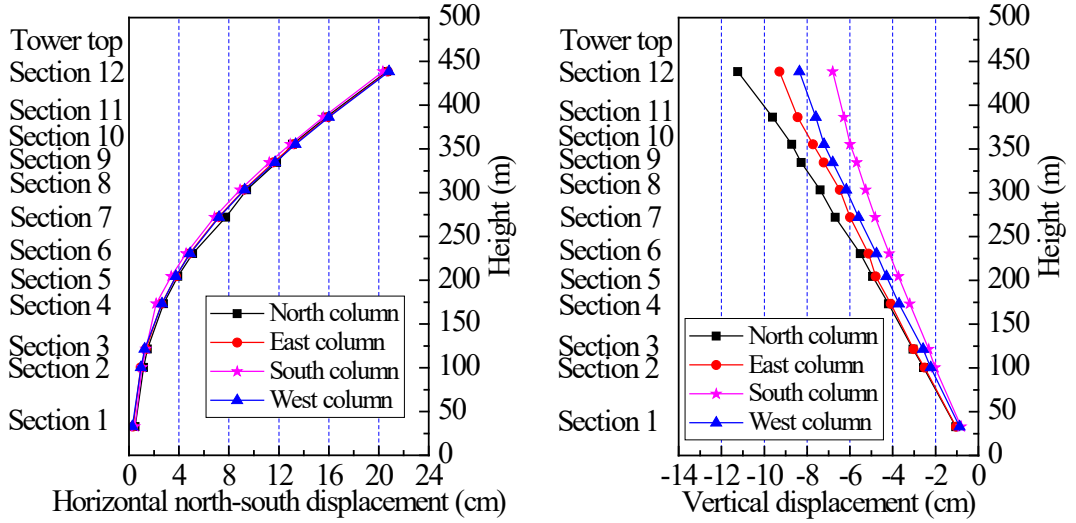

(b)

Figure 23. Simulated temperature-induced displacement profile of the inner and outer tubes in Case 5: (a) inner tube and (b) outer tube

In the vertical direction, the outer columns had a larger vertical displacement than the inner tube because the outer tube had a larger temperature decrease from summer to winter than the inner tube. The different facades also had different vertical displacements. In particular, the north and east facades had larger downward displacement than the south and west facades. This finding is consistent with the observation that the tower leaned toward the northeast. Thus, the horizontal cross-section had an inclination. The maximum vertical displacement difference is approximately 1.4 cm in the inner tube and 4.4 cm in the outer tube, occurring between the north and south facades.

6.3. Temperature-induced stress

Figure 24 shows the calculated variations in the stresses of Points 1 to 4 at different heights between Cases 1 and 3, when the structure has the highest temperature in the summer and the lowest temperature in the winter, as compared with the measured counterparts. The variation of stress changed significantly in the transition sections between the zones with and without functional floors (Sections 2, 9, and 11), which is consistent with the measured results. The largest measured variation in stress was observed at Point 2 of Section 2 with approximately −2.8 MPa, accounting for approximately 25% of the total stress.

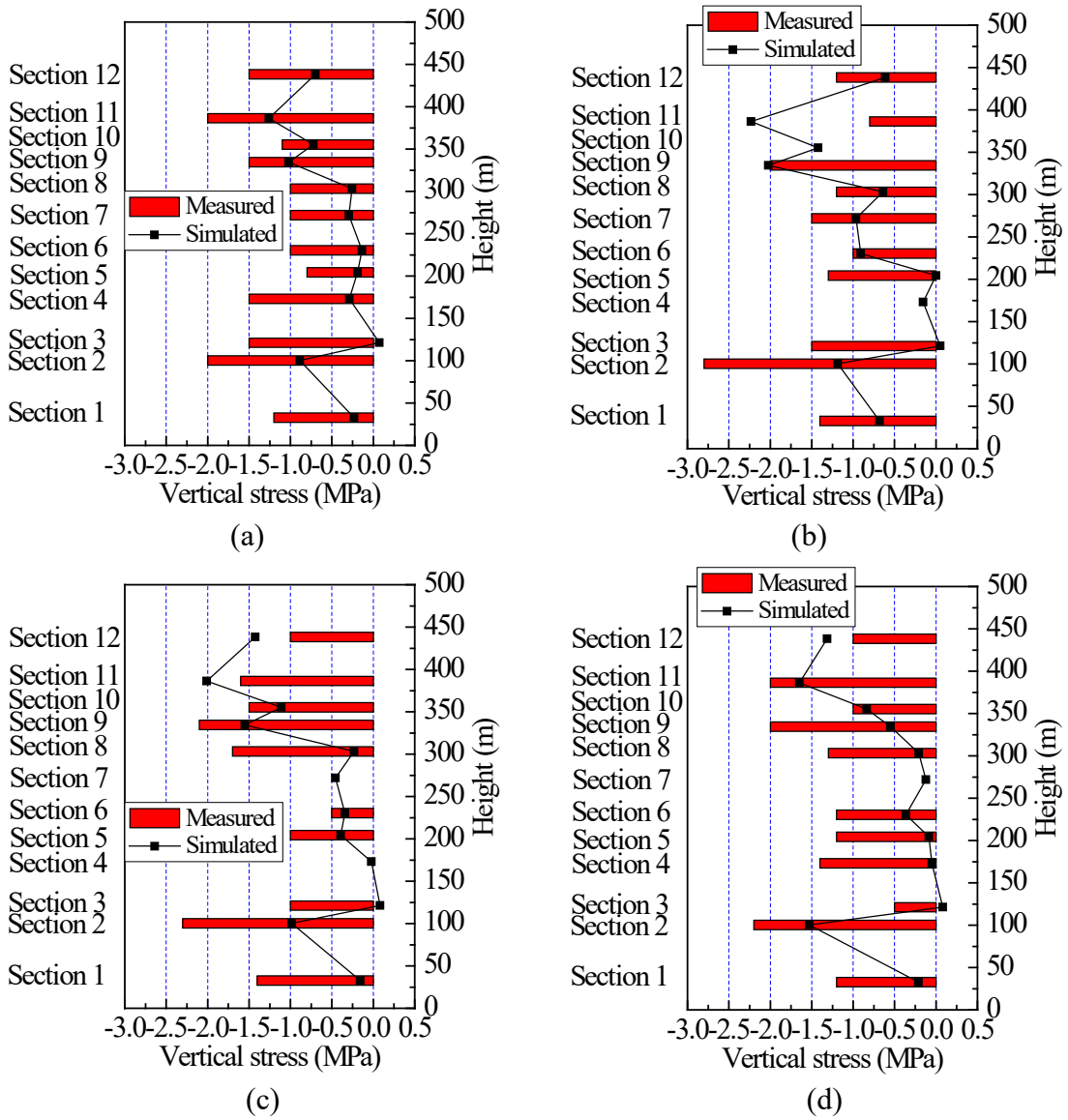

Figure 24. Simulated and measured stress variations of the inner tube from summer to winter: (a) Point 1, (b) Point 2, (c) Point 3, and (d) Point 4

The simulated and measured tendencies of the stress change along the height of the tower are generally consistent, although several discrepancies can be observed in the segments where the inner tube connects with the functional floors. The main reason may be the inaccuracy of the temperature data used in the simplified FE model. For example, the temperature distribution of the floor slabs is assumed to be uniform, as no sensor has been installed on the floors. Measurement noise may be another reason.

Figure 25 compares the simulated and measured stress variation profiles of the outer tube between Cases 1 and 3. The stresses of the CFT columns on the northeast facade decreased, whereas those on the southwest facade increased. The tower leaned toward the northeast from summer to winter, resulting in increased compression of the columns on the northeast. The stresses of the columns in the southwest significantly increased by 1.2 MPa, which accounted for approximately 11% of the total stress. The largest stress decrease occurred at the column in the northeast. The simulated stress variations of several columns differ from the measured values because of the modeling error of the temperature distribution and the measurement noise.

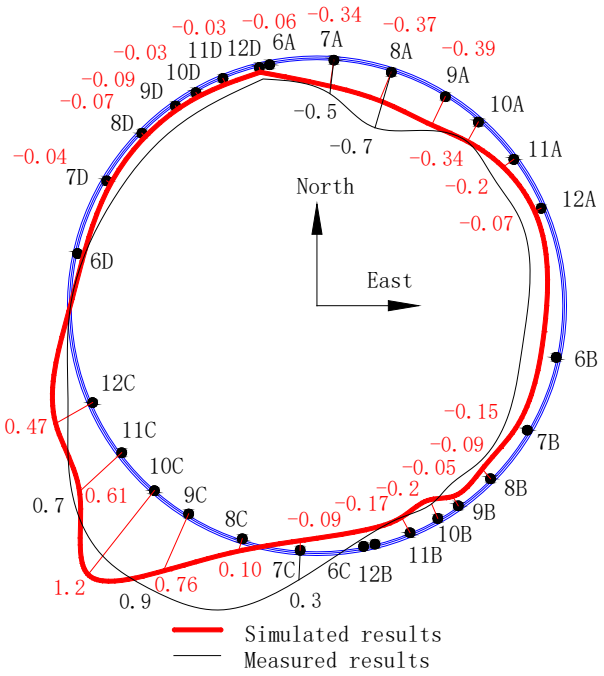

Figure 25. Simulated and measured stress variation profiles of the outer tube from summer to winter (unit: MPa)

6.4. Temperature-induced internal forces of beams

The temperature-induced axial shortening differences of the walls and columns in a high-rise structure not only causes axial force redistribution among them but also produces additional bending moments and shear forces in the horizontal members, such as beams and slabs. Figure 26 illustrates the profiles of the bending moment and shear force induced by the temperature decreasing from summer (Case 1) to winter (Case 3) and the ratio of these variations to the corresponding forces under the dead load. The maximum value among all horizontal girders on each floor of the tower is presented in the figure. The temperature-induced bending moment and shear force of the beams at the highest story and those of the connection girders at the middle of the tower are larger than the forces of other segments. This finding is attributed to the fact that the largest vertical deformation difference between the inner and outer tubes usually accumulates in the upper stories, generating the larger bending moment and shear force in the beams of these floors. This scenario is different from other loading effects, for example, the wind loading, which generally causes the maximum forces at the bottom of the structure. For the segment without functional floors at the middle of the tower, only four levels of the connection girders link the inner tube to the outer tube. This segment is the weakest along the structural height. These girders are also subject to large thermal actions. The temperature-induced bending moment and shear force can reach 72% and 56% of those induced by the dead load, respectively. Therefore, special attention should be paid to the thermal loading, particularly for this type of complicated supertall structures.

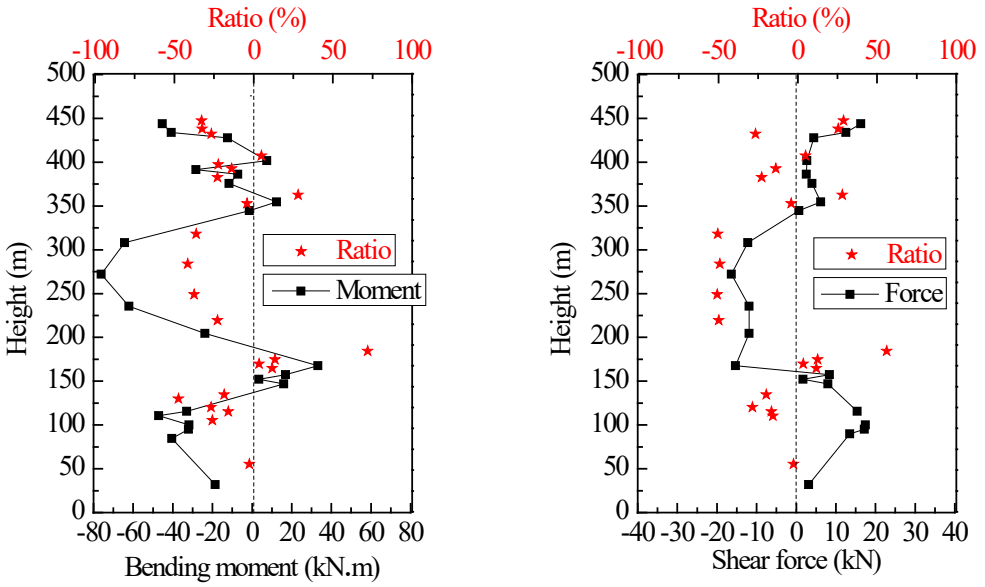

Figure 26. Calculated beam-end bending moment and shear force from summer to winter

7. CONCLUSIONS AND DISCUSSIONS

Accurately obtaining the temperature distribution of supertall buildings is a challenge because of complex configurations and highly uncertain and varying meteorological environments. The densely distributed temperature and strain sensors in the Canton Tower are used in this study to investigate the thermal action of this supertall structure. Based on the five-year field monitoring data during the service stage of the structure, the following results have been obtained:

1 The ground ambient air temperature ranges from 2 °C to 40 °C. The average air temperature decrease rate is approximately 6.7 °C/km as the altitude increases. The effective temperature of the structure ranges from 6 °C to 32 °C for the inner tube and from 1 °C to 36 °C for the outer tube.

2 The maximum temperature difference between the outer CFT tube and the inner RC tube is −15.0 °C in the winter and 8.1 °C in the summer for the inner tube enclosed by the curtain wall. For segments where the outer and inner tubes are exposed to the environment, the corresponding maximum difference is −6.0 °C in the winter and 2.0 °C in the summer. Recommendations for the distribution of their differences along the structural height are proposed.

3 The temperature difference between different facades of the inner tube enclosed by the curtain wall is negligible, whereas the temperature difference of the segments where the inner tube is exposed to the environment cannot be ignored.

4 In the outer tube, the south facade has higher temperature than the north facade, and the maximum difference is approximately 7 °C. The temperature difference profiles among different facades are obtained.

5 The peak-to-peak tower top motion throughout a sunny day in winter was 15.7 cm in the east–west direction and 15.5 cm in the south–north direction, and the maximum displacement was approximately 20 cm. From summer to winter, the overall tower leaned toward the northeast and the tower top motion is approximately 15 cm in the horizontal direction. The tower had a larger daily horizontal displacement in the winter than that in the other seasons. The temperature-induced displacement at the tower top was also calculated by using the FE model. The results show a good consistency with the measured data.

6 The temperature variations cause the stresses of the different members of the entire structure to redistribute. In particular, the temperature-induced vertical stresses of the inner tube increased as temperature increased from winter to summer. The compressive stress of the CFT columns on the northeast facade decreased, whereas that on the southwest facade increased from winter to summer. The temperature-induced stress change in different seasons can reach 25% of the total stress for the inner tube and 11% for the outer tube.

7 The temperature difference between the inner and outer tubes produces significant bending moment and shear force in the beams linking the inner tube to the outer tube. The internal forces of the highest stories are larger than those of the lower stories because the vertical deformation difference between the inner and outer tubes accumulates at the upper stories, generating the larger internal forces in these floors. This characteristic is different from other loading effects which generally cause largest force in the bottom of the structure.

The temperature behavior of a supertall structure is complex. The temperature pattern

obtained in this study may not necessarily represent other structures. The temperature characteristics depend on the structural configurations, construction materials, meteorological conditions, and geographical locations. Nevertheless, the analysis procedures used in this study are applicable to other studies, and the results can be used as reference for the design of similar structures in the future. With additional monitoring exercises implemented in practice, the temperature behavior of high-rise structures can be more accurately understood and codified.

ACKNOWLEDGMENTS

This research was supported by the Research Grants Council of the Hong Kong Special Administrative Region, China (Project No. PolyU 5285/12E) and NSFC Joint Research Fund for Overseas and Hong Kong and Macao Scholars (Project No. 51328802).

REFERENCES

1. Kennedy J, Soliman M. Temperature distributions in composite bridges. *Journal of Structural Engineering* 1987; **113**(3):65–78.
2. Malla R, Nash W, Lardner T. Thermal effects on very large space structures. *Journal of Aerospace Engineering* 1988; **1**(3):171–188.
3. Zhou LR, Xia Y, Brownjohn JMW, Koo, KY. Temperature analysis of a long-span suspension bridge based on field monitoring and numerical simulation. *Journal of Bridge Engineering ASCE* 2016; 21 (1): 040150275.
4. Xia Y, Xu YL, Wei ZL, Zhu HP, Zhou XQ. Variation of structural vibration characteristics versus non-uniform temperature distribution. *Engineering Structures* 2011; **33**(1):146–153.
5. Xia Y, Zhang P, Ni, YQ, Zhu, HP. Deformation monitoring of a super-tall structure using real-time strain data. *Engineering Structures* 2014; **67**:29–38.
6. Eurocode-1. *EN 1991-1-5. Actions on Structures. Part 1–5: General Actions − Thermal Actions*. European Committee for Standardization, Brussels, Belgium, 2003.
7. Xia Y, Chen B, Zhou XQ, Xu YL. Field monitoring and numerical analysis of Tsing Ma suspension bridge temperature behavior. *Structural Control and Health Monitoring* 2013; **20**(4):560–575.
8. Zhou GD, Yi TH. Thermal load in large-scale bridges: a state-of-the-art review. *International Journal of Distributed Sensor Networks* 2013; **2013**:1–17.
9. McLaughlin ER. Temperature effects on tall steel framed buildings Part 1 - Response of steel columns to temperature exposure. *National Engineering Conference AISC*, Pittsburgh, USA, 1970; **7**(4):105–109.
10. West HH, Kar AK. Temperature effects on tall steel framed buildings Part 2 - Structural analysis. *National Engineering Conference AISC*, Pittsburgh, USA, 1970; **7**(4):110–120.
11. Khan FR, Nassetta AF. Temperature effects on tall steel framed buildings Part 3 - Design considerations. *National Engineering Conference AISC*, Pittsburgh, USA, 1970; **7**(4):121–131.
12. Pirner M, Fischer O. Long-time observation of wind and temperature effects on TV towers. *Journal of Wind Engineering and Industrial Aerodynamics* 1999; **79**(1-2):1–9.
13. Tamura Y, Matsui M, Pagnini LC, Ishibashi R, Yoshida A. Measurement of wind-induced response of buildings using RTK-GPS. *Journal of Wind Engineering and Industrial Aerodynamics* 2002; **90**(12–15):1783–1793.
14. Seco A, Tirapu F, Ramirez F, Garcia B, Cabrejas J. Assessing building displacement with GPS. *Building and Environment* 2007; **42**(1):393–399.
15. Breuer P, Chmielewski T, Gorski P, Konopka E, Tarczynski L. The Stuttgart TV Tower-displacement of the top caused by the effects of sun and wind. *Engineering Structures* 2008; **30**(10):2771–2781
16. Breuer P. Monitoring the horizontal displacement of slim high towers caused by daily temperature variation and wind impact by application of static and kinematic GPS-Mode: some results. *Proceedings of the 5th World Conference on Structural Control and*

Monitoring 2010, Tokyo, Japan.
17. Azkune M, Puente I, Insausti A. Effect of ambient temperature on the redistribution of loads during construction of multi-storey concrete structures. *Engineering Structures* 2007; **29**(6):933–941.
18. Zheng YM, Zhang PP, Zhao X, Zheng Y. Analysis on sunshine temperature difference effect of Shanghai Center. *Building Structure* 2011; **41**(5):28–32. (in Chinese).
19. GB 50009-2012. *Load Code for the Design of Building Structures*. China Architecture and Building Press, Beijing, China, 2012.
20. Xia Y, Ni YQ, Zhang P, Liao WY, Ko JM. Stress development of a super-tall structure during construction: field monitoring and numerical analysis. *Computer-Aided Civil and Infrastructure Engineering* 2011; **26**(7): 542–559.
21. Ni YQ, Xia Y, Liao WY, Ko JM. Technology innovation in developing the structural health monitoring system for Guangzhou New TV Tower, *Structural Control and Health Monitoring* 2009; **16**(1):73–98.
22. Howell JR., Siegel R, Menguc MP. *Thermal Radiation Heat Transfer, Fifth Edition*, CRC Press, Taylor & Francis Group, 2011.
23. Computers and Structures Inc., *SAP2000 Linear and Nonlinear Static and Dynamic Analysis and Design of Three-Dimensional Structures*", Berkeley, California, USA, version 14.0, 2009.
24. Geokon 4200, http://www.geokon.com/products/datasheets/4200.pdf
25. Geokon 4000, http://www.geokon.com/products/datasheets/4000.pdf
26. Jacobson MZ. *Fundamentals of Atmospheric Modeling*, second edited, Cambridge University Press, 2005.
27. Li DN, Maes MA, Dilger WH. Thermal design criteria for deep prestressed concrete girders based on data from Confederation Bridge. *Canadian Journal of Civil Engineering* 2004; **31**:813–825.
28. Zhou HF, Ni YQ, Ko JM. Constructing input to neural networks for modeling temperature-caused modal variability: mean temperatures, effective temperatures, and principal components of temperatures. *Engineering Structures* 2010; **32**(6):1747–1759.
29. Lienhard JH, Lienhard JH. *A Heat Transfer Textbook*, third edited, Phlogiston Press, Cambridge, Massachusetts, USA, 2003.
30. ANSYS 10.0 [Computer software], ANSYS Inc., Southpointe, PA, USA, 2005.